

Chapter 17

Calorimeter

This chapter illustrates the design concept for the 24 electromagnetic calorimeters. The primary purpose of the electromagnetic calorimeter is to measure the energy and time of arrival of the daughter positrons from stored muon decay. The physics goals and subsequent requirements are reviewed. The recommended design for each subsystem — Absorber, Photodetection (SiPM), Bias Control, Laser Calibration, and Mechanical — is then presented. Finally, alternative designs, ES&H, risks, quality assurance, and value management are discussed.

17.1 Physics Goals and Requirements

After a muon decays into a positron and a neutrino, the positron doesn't end up with sufficient energy to fly along the magic orbit in the ring. It curls inward where it hits a segmented *lead fluoride calorimeter* readout by *silicon photo-multipliers* (SiPM). The primary physics goal of the calorimeter is to measure energy and hit time of daughter positrons.

The requirements on the energy and time measurements are:

- Relative *energy resolution* of the reconstructed positron energy summed across calorimeter segments must be better than 5% at 2 GeV. The modest specification on energy resolution is motivated by the purpose of the energy measurement which is to select events. Deposited energy is not a direct observable in the experiment.
- *Timing resolution* of the hit time extracted from the fit of the SiPM current pulse must be better than 100 ps for positrons with kinetic energy greater than 100 MeV in any combination of temporal and spatial pileups.
- The calorimeter must be able to *resolve* two *showers* by temporal or spatial separation. The calorimeters must provide 100% efficiency in the discrimination of two showers with time separations greater than 5 ns. Showers that occur closer in time than 5 ns must be further resolved spatially in more than 66% of occurrences. These requirements correspond to the systematic uncertainty on unidentified pileup events of 40 ppb.
- The *gain (G) stability* requires a maximally allowed gain change of $\frac{\delta G}{G} < 0.1\%$ within a 200 μ s time period in a fill. In addition, the arrival of a pulse should not affect the

gain for a second pulse arriving a few nanoseconds later on the same channel, unless that change is understood and can be applied to the interpretation of a following pulse in a reliable manner. The long term gain stability (intervals of multiple seconds) is more relaxed and must be $\frac{\delta G}{G} < 1\%$. To verify the overall gain stability, each of the 24 stations must be equipped with a calibration system that must monitor the gain continually during the muon spills with a precision of $\frac{\delta G}{G} \sim 0.04\%$. These requirements correspond to the systematic uncertainty on rate dependent gain effects of 20 ppb.

- Efforts must to be made to preserve *fidelity* of the Cerenkov light *pulse shape* through the analog and digital signal chain.

17.2 Evaluation Methodologies

The baseline calorimeter design builds upon extensive testing and simulation efforts. Prototype detectors were built. Various silicon photomultiplier (SiPM) and photomultiplier tube (PMT) candidates were tested. Several iterations of the electronics boards needed to operate the SiPMs were built and tested. Both laboratory and test beam studies were performed. We employed simulations to study detector performance, sensitivity to ω_a and pulse-shape fitting.

17.2.1 Test beams

Laboratory tests with beams and lasers provided crucial results on pulse shape and energy resolution for different component choices, and also validated and informed our simulation efforts. The Fermilab Test Beam Facility (FTBF) was used several times to evaluate prototype calorimeters. In particular, our first effort in which 0.5-mm pitch tungsten plates alternated with 0.5-mm layers of scintillating fiber resulted in a publication [2]. A larger prototype was then built and tested, see Fig. 17.1.

The recommended design based on PbF_2 crystals was tested using the 7-crystal array shown in Fig. 17.1. These crystals were compared directly to the W/SciFi detector and to a custom PbWO_4 crystal during the April 2012 FTBF period. The right panel of Fig. 17.1 shows the arrangement of PbF_2 crystals during assembly and displays a front view of the full test setup. Various readout methods, wrappings and couplings were employed.

Two test beam evaluations of advanced PbF_2 calorimeter prototypes were completed at SLAC National Accelerator Laboratory's End Station Test Beam facility. The SLAC prototypes included SiPM photodetectors with custom amplifier boards designed by electrical engineers at the University of Washington. In both tests, SLAC provided an electron beam with energies ranging from 2.5 to 4 GeV, similar to the energies we expect from decay electrons in the final experiment. Scanning over this range of electron energies enabled evaluation the calorimeter's energy resolution and linearity.

The first test occurred in November of 2013 and featured a 3×3 array of crystals; the second occurred in July of 2014 and featured a larger 4×7 array. Both of these tests were highly successful in confirming the baseline calorimeter's ability to meet its design requirements. In order to investigate the effects of different wrapping types on the detector response, the 4×7

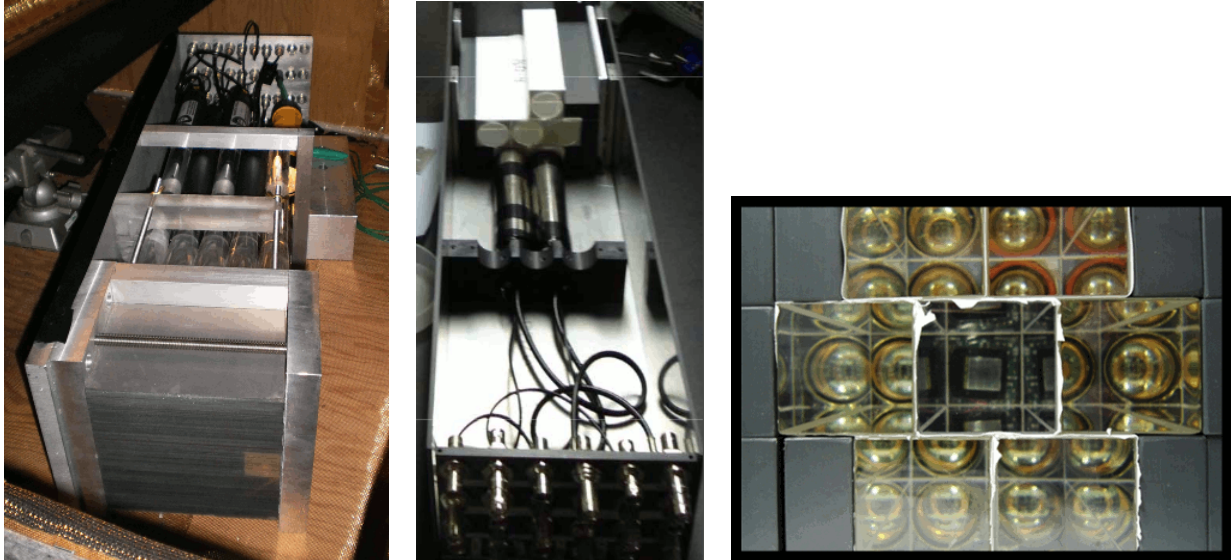


Figure 17.1: Left: Monolithic block of W/SciFi having 0.5 mm thick pure tungsten plates alternated with 0.5 mm diameter ribbons of blue scintillating fiber. The readout side is divided into 25 individual elements. Tapered light-guides direct the light from a 3×3 cm² area to a PMT. Center: Crystals being prepared for test beam. Here, PMTs are used for the outer elements and a SiPM will be placed on the center crystal and alternatively a very fast Hamamatsu R9800 PMT for comparison. Right: Front picture of the 7-crystal test array used in the FTBF. In this configuration, a SiPM is visible on the center channel, while PMTs are used on the remaining elements. These crystals were wrapped in white Millipore paper.

array used in 2014 was prepared as a 4×4 array of white, reflective paper wrapped crystals adjacent to a 4×3 array of black, absorptive paper wrapped crystals. Results from the 2014 test beam experiment have been published [3]. This document will focus on results from the 2014 test because the design and techniques applied there incorporated lessons learned from the 2013 test.

A light-tight housing for the tested prototype was constructed by CENPA engineers and featured a cold-air temperature stabilization system that was required to maintain acceptable SiPM gain stability. A cooling concept based on pressurized chilled and dried air blowing directly on SiPM boards was commissioned during this test run. While it successfully provided stability, the achieved temperature uniformity was not great and the system would be difficult to implement in the final design. A new water-cooling design is under preparation for the final calorimeter housing. Signals from the SiPMs were fed into a pair of Struck's 4-channel SIS3350 500MS/s 12-bit digitizers and a CAEN DT5742 16-channel 12-bit digitizer running at 1 GS/s.

The SLAC test provided an invaluable opportunity to test the calorimeter's laser calibration system. At the center of the calibration system is a PicoQuant pulsed diode laser, distributed through fiber optics to each crystal, and ultimately each SiPM, individually. A remote controllable neutral density filter wheel is placed in the path of the laser beam and used to vary the pulse energy seen by the calorimeter. By observing how the statistical width

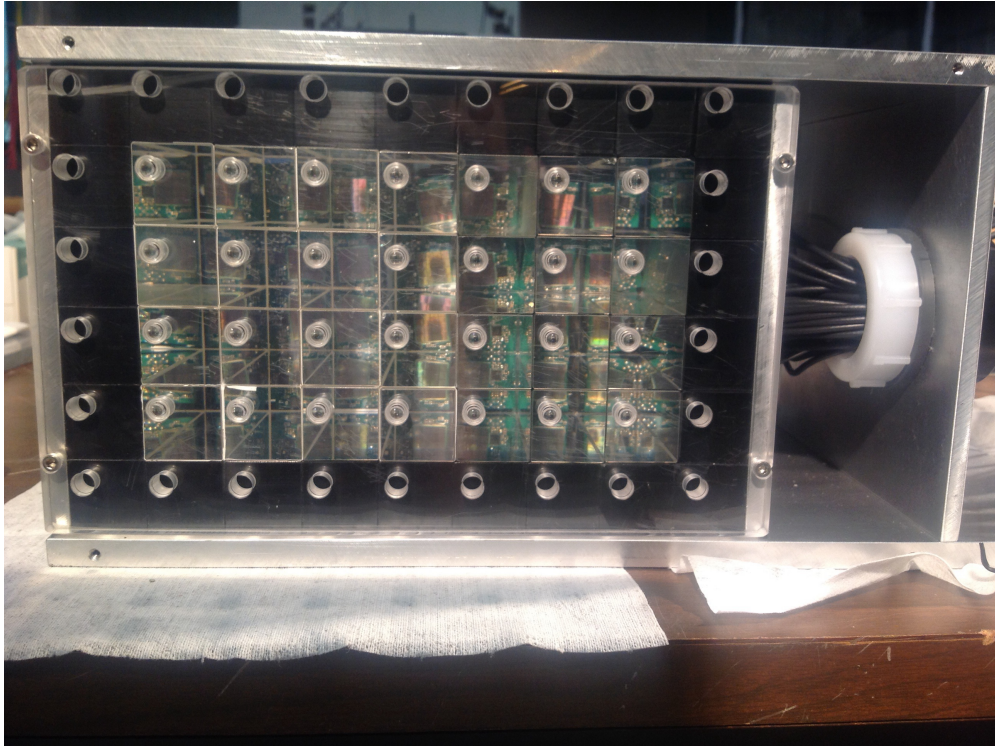


Figure 17.2: A calorimeter test-box was used at SLAC to measure the light yield of lead fluoride, better understand SiPM photo-efficiency, and characterize energy resolution. Analysis of data obtained using this test-box proved that our design meets $g - 2$ requirements.

of the reconstructed energy distribution in each SiPM varies with the mean, one can obtain relative calibration constants for each of the calorimeter segments. In principle, this technique does not rely on each fiber delivering the same amount of light, as long as the light level is low enough that the SiPM responses can be treated as linear. Once relative calibration constants are established, long term stability is ensured by periodically firing a fixed-energy laser pulse into every segment. Undesired fluctuations in laser pulse energy are corrected for by a suite of dedicated laser monitors. These techniques produced a reconstructed energy that was independent of both time and impact position and revealed that our calorimeter yields (1.45 ± 0.05) pe/MeV when the crystals are wrapped in white, reflective paper and (0.76 ± 0.04) pe/MeV when the crystals are wrapped in black, absorptive paper (fig. 17.3).

In order to achieve accurate energy measurements and the best resolution, the energy seen by each detector must be summed together on an event by event basis. For linearity and resolution tests, sums were taken over 3×3 sub-arrays. The sums were executed using calibration constants obtained with the aforementioned laser system.

After conducting energy sums across our array, we were able to demonstrate that the *energy resolution* of our calorimeter exceeds the requirement of 5% at 2 GeV for both white and black wrapped crystals, see fig. 17.4. An energy scan in the 2.5–4.0 GeV range, depicted in fig. 17.3, proved an excellent linearity of the PbF₂ calorimeter.

The SLAC facility featured a remote controlled x–y table that allowed us to scan the beam over the face of our detector. Our reconstructed energy was independent of the beam

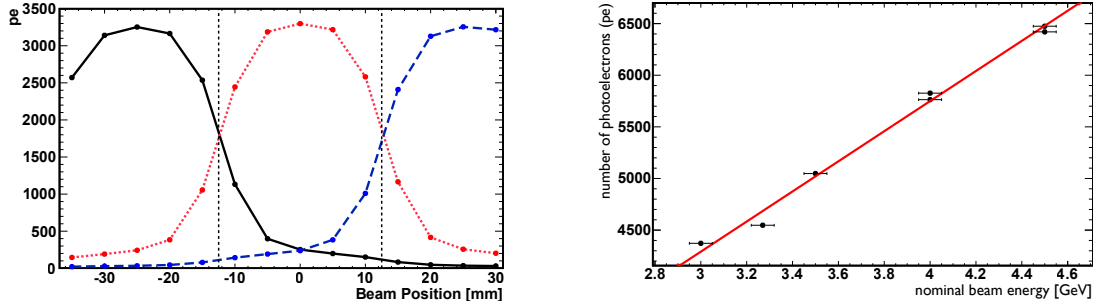


Figure 17.3: Left: Reconstructed energy in three adjacent crystals as the electron beam is scanned across. The calibration constants obtained from the technique described in the text bring their peaks to the same height. pe stands for photoelectrons. Right: Measured pe in a 3×3 cluster of crystals wrapped in white, reflective paper as a function of nominal beam energy. The uncertainties on the nominal beam energies are set to 50 MeV, the stated confidence of the beam operators. Absolute scale is obtained from the laser calibration and allows an extraction of pe/MeV.

position and incident angle (we tested up to 20°). By examining the distribution of energy between crystals we were able to locate the beam position. This segmented nature of the detector contributes significantly to its pileup resolution capabilities. Additionally, the test beam was used to investigate the calorimeter system's long term gain stability. Using the techniques described above, we found that gain stability is correctable to better than 10^{-4} /hour (fig 17.5).

17.3 Lab tests

Timing response of SiPMs was studied using a 407 nm pulsed diode laser. A laser shot was split into two channels, one of them was optionally delayed and fed through crystals into two different SiPMs. The hit times were extracted from pulse fits. An experiment was repeated many times, and a histogram of these time differences was created. The histogram was well fit with a Gaussian distribution, with mean value identical to the known delay between the two laser shots, and with the sigma of 40 ps. The sigma was independent of pulse heights. The same study was repeated for the pileup events: both the prompt and delay pulses were fed into a single crystal read by a SiPM. Also in this case, the histogram of hit time differences was statistically compatible with the Gaussian distribution, its mean value was not biased, and the sigma turned was 70 ps. Both the studies were performed with 500 MHz digitizers. This timing response meets the experimental requirements. Upgrading from 500 MHz to 800 MHz in the final digitizer design will likely further improve the timing response.

SiPM *bulk recovery time* (temporary bias voltage drop) was understood in a dedicated systematics study. An Agilent 33521A function generator was used to generate LED pulses at a rate of $1 \cdot \exp(-t/\tau_\mu)$ MHz, where τ_μ is the boosted muon lifetime of about $64.4 \mu\text{s}$. This setup simulates a $(g - 2)$ muon fill. At an adjustable time during this fill, the SiPM was illuminated with a fixed-energy 407 nm laser shot and the resulting pulse was digitized

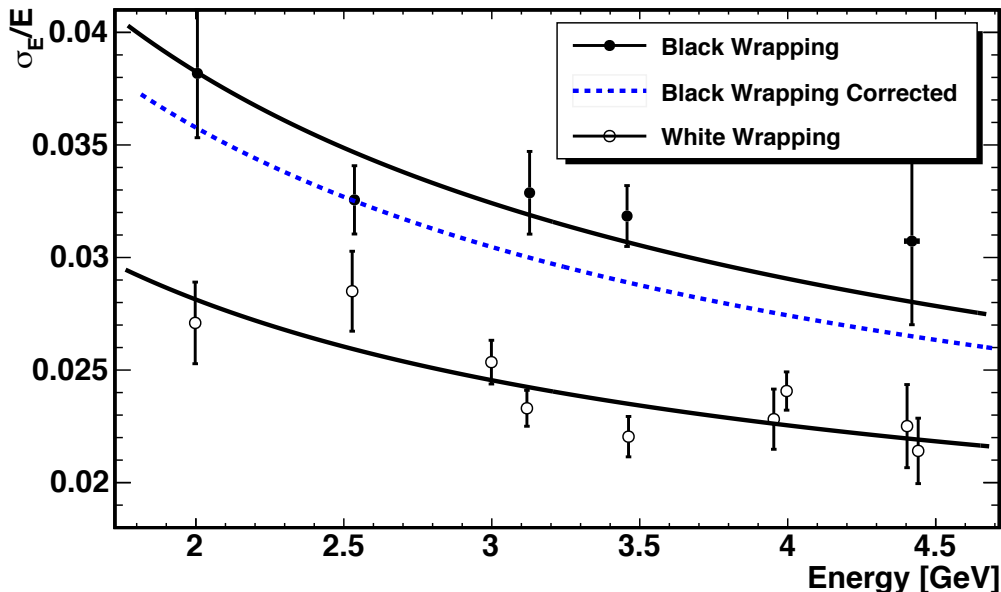


Figure 17.4: Energy resolutions of 3×3 arrays of PbF_2 crystals with black and white wrappings as a function of energy. Fit functions are of the form $\sigma_E^2/E^2 = (1.5\%)^2 + a^2/E$. The blue dashed line is the result of correcting the black-wrapped curve for dead channels SiPM channels discovered after the fact.

and recorded. By observing the SiPM response to a fixed-energy laser shot at varying times during and outside of a simulated fill, the SiPM average gain function, $G(t)$, can be extracted. The energy of the LED pulses was also varied to investigate how $G(t)$ changes with average current; it was determined that $G(t)$ scales linearly with average current in the relevant regime.

It was shown in section 16.3.1 that the target value for gain perturbations during the fill is $< 10^{-3}$. The result of this test, shown in fig. 17.6, is that the current SiPM boards meet the experimental systematic error requirement of gain stability better than 10^{-3} during the fill.

17.3.1 Calorimeter rate simulation

It is instructive to estimate the event rate for a single calorimeter station and for the hottest element of the designed array of 54 crystals. The average number of positrons above an energy threshold E incident on a calorimeter at a fixed time after injection follows the form given in Equation 17.1. Here $N_\mu(E)$ is the number of muons that decay to positrons above energy E and $\epsilon(E)$ is the calorimeter acceptance. Using the expected number of stored muons per fill of $\sim 16,000$ (see Chapter 5) and the acceptance derived from our full GEANT-based simulation [6], we find the average rate at the fit start time of $31 \mu\text{s}$ to be nearly 3 MHz for a full calorimeter, as shown by the solid black line in Fig. 17.7. What the detector experiences is the local instantaneous rate, which is modulated by two frequencies. The first is the normal $g-2$ frequency having period $\sim 4360 \text{ ns}$. The modulation depends on the asymmetry, $A(E)$ as parameterized in Eq. 17.2. For a threshold as low as 100 MeV, the asymmetry is small

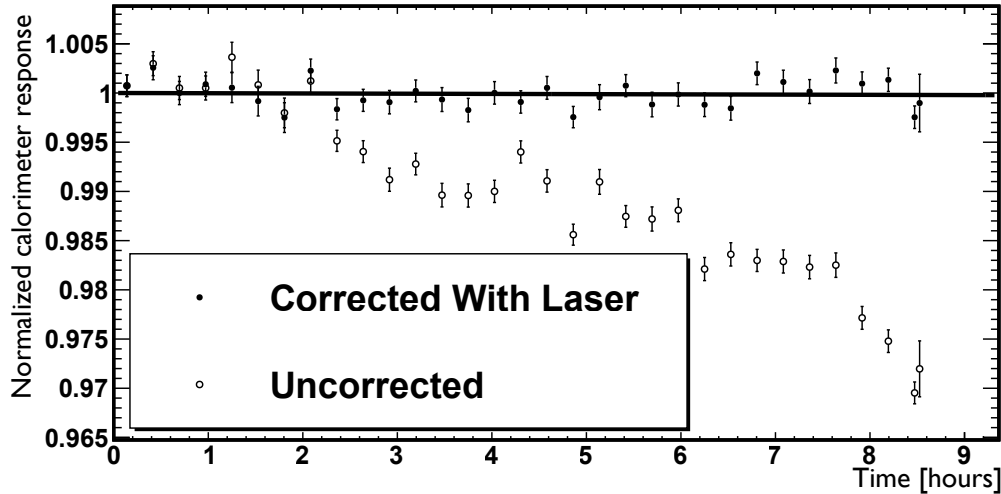


Figure 17.5: Reconstructed energy, normalized to 1, from a 3 GeV electron beam firing continually over a 9 hour period. After correction with the laser system, the reconstructed energy is stable at the level of 10^{-4} /hour.

and the resulting rate is shown by the solid blue line in Fig. 17.7. The “in-phase” peak rate rises compared to the average value by a small factor.

$$R_{\text{exp}}(E, t) = N_{\mu}(E) \cdot \epsilon(E) \cdot (\gamma\tau_{\mu})^{-1} \exp(-t/\gamma\tau_{\mu}) \quad (17.1)$$

$$R_{g-2}(E, t) = R_{\text{exp}} \cdot [1 + A(E) \cos(\omega_a t)] \quad (17.2)$$

$$R_{\text{FR}}(E, t) = R_{g-2} \cdot [1 + A_c \exp(-t/\tau_{\text{FR}}) \cos(\omega_c t)] \quad (17.3)$$

More importantly is the effect of the time-structured beam profile at injection. The ~ 80 ns flat-top of the kicker will efficiently store the central portion of the ~ 120 -ns-long entering beam bunch. As this bunch rotates at the cyclotron frequency, $\omega_c = 149$ ns, a large intensity oscillation will be imprinted on the distribution. Using a simplified model with a cosine dependence, this “fast-rotation” effect can be described by an amplitude, A_{FR} , a damping time constant τ_{FR} , and the cyclotron frequency ω_c . The damping occurs as the beam spreads out owing to the momentum dispersion. An effective damping factor is used based on the E821 experiment. The final rate is described by Eq. 17.3 and is depicted by the solid red envelope in Fig. 17.7 Note that $\omega_c \gg \omega_a$. The peak rate rises at fit start to about 4 MHz.

Unlike E821, detectors in E989 will not be gated off during injection. Therefore both the average and instantaneous rates at $t = 0$ in Fig. 17.7 are useful guides for planning purposes.

Table 17.1: Projected Rates in Calorimeters

Region	ϵ	Instantaneous Rate	$\sim N_{\text{stored}}$
Full Calorimeter ($E > 100$ MeV)	0.0191	2.9 MHz	linear
Hot Crystal ($E > 25$ MeV)	0.0031	0.48 MHz	linear
Hot Crystal Pileup Fraction	–	0.24%	quadratic

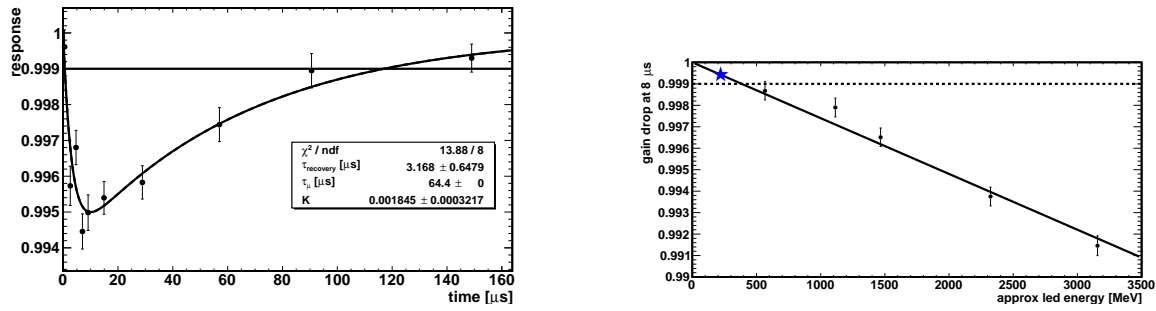


Figure 17.6: Left: Results from lab test measuring SiPM $G(t)$. The vertical axis shows the ratio of SiPM pulse area during an LED fill to pulse area outside of an LED fill, where an LED fill is described in the text. The minimum of this function occurs at $\sim 8 \mu\text{s}$. Right: $G(8 \mu\text{s})$ scaling as energy of LED shots during the LED fill is varied. The scaling is linear. The blue star denotes the average pulse energy expected in $(g - 2)$, the dashed line denotes the experimental goal. Extrapolating LED energy to the expected $(g - 2)$ energy indicates that our system exceeds the design requirement.

The instantaneous rates are summarized in Table 17.1. The term “Full Calorimeter” is the rate as if the entire calorimeter were readout as one monolith. The crystal where the maximum rate is expected is called the “Hot Crystal.” A crystal is assumed to be hit if it absorbs more than 25 MeV in any event, no matter where the incoming positron strikes. Figure 17.8 shows the instantaneous rate of hits over 25 MeV for each individual calorimeter crystal in the array.

Finally the fractional rate of pileup is also calculated for the hot crystal. The pileup rate is given by

$$\langle R_{\text{pileup}} \rangle = \langle R \rangle^2 \cdot \Delta t \quad (17.4)$$

where Δt is the resolving time of the calorimeter. Working with the rate in the hot crystal and a resolving time of 5 ns we calculate the maximum pileup fraction to be 0.24%, or a rate of about 1 kHz.

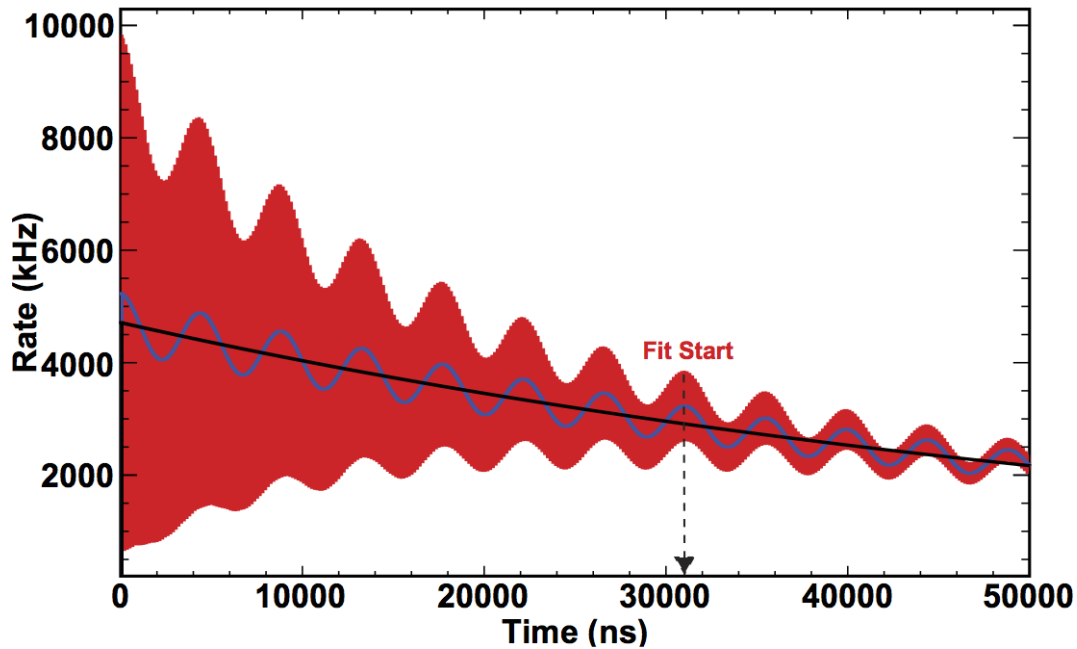


Figure 17.7: The three curves represent the instantaneous rate for: decaying muons (black), with ω_a oscillation (blue), and with fast rotation (red). This data was simulated using the standard run conditions outlined in the TDR and a low-energy threshold of 100 MeV. This plot is for one calorimeter station.

17.4 Baseline calorimeter design

The calorimeter system includes the following subsystems: absorber, photodetection, bias control, calibration, and mechanical. Over the past several years, the calorimeter design has gone through an extensive down-select process for absorber and readout technologies.

- *Absorber:* Each of the 24 calorimeter stations consists of a 6×9 array of lead fluoride (PbF_2) Čerenkov crystals. The crystal is $25 \times 25 \times 140 \text{ mm}^3$, and wrapped in a single layer of highly reflective Millipore paper.
- *Photodetector:* Each crystal is read out by a monolithic 16-channel Hamamatsu MPPC (S12642-0404PA-50). (Multi-Pixel Photon Counter, also called silicon photomultipliers or SiPM's). This SiPM has an active area of $12 \times 12 \text{ mm}^2$, and 57 344 $50\text{-}\mu\text{m}$ pixels. The current pulse output by SiPM is amplified and converted into a voltage signal in a custom made amplifier board that the SiPM is soldered to. The output stage of the amplifier board features a digitally controlled variable gain amplifier which is AC coupled to a differential pair of coaxial cables to avoid ground loops, and maximize signal to noise ratio. The recommended design does not include pole zero correction, or any other tool to shape the output pulse. Preserving the intrinsic Čerenkov light pulse shape is among our goals. The light yield of the crystals is MC-predicted and measured to be 1.0 registered photo-electrons per 1 MeV of deposited energy.

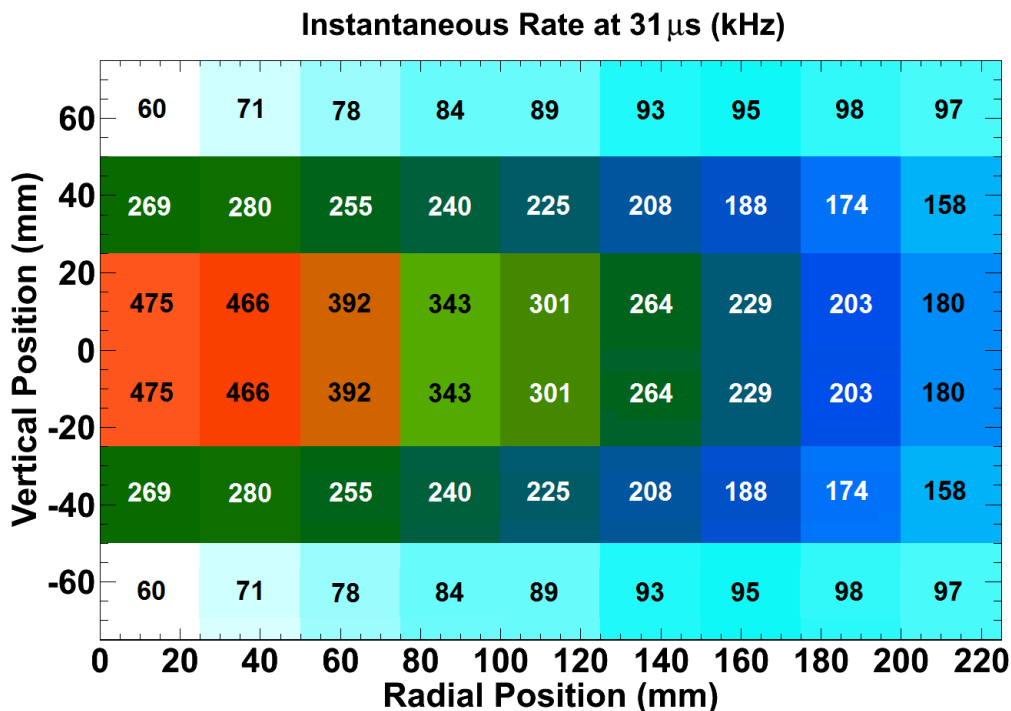


Figure 17.8: Projected instantaneous rate in each calorimeter crystal 31 μs after muon injection. Individual crystal acceptance was calculated from a GEANT simulation with showering and energy deposition in the crystals. A threshold of 25 MeV was applied in analysis to act as a hardware threshold. The acceptances were then combined with the overall rate scale outlined in the TDR to determine the rate in each crystal. The smaller radial positions are closer to the muon storage region, as seen by the enhanced rate.

- *HV bias control:* Reverse bias voltage applied to a SiPM is provided by a commercial HV bias power supply that maintains better than 1 mV stability over the critical 700 μs time window. The voltage output ranges from 60 V to 80 V, and can be set digitally. Each output channel will serve about 12 SiPMs, allowing four or five individually tunable bias values per calorimeter.
- *Laser calibration:* The calorimeter gain is calibrated and continuously monitored by a state-of-the-art high-performance laser-based distributed system. The unique system is critical to keep systematic contributions from any energy-scale instability well below the statistical precision of the measured ω_a frequency. Additionally the system will be used to initially tune and set gains for all crystals.
- *Mechanical:* A calorimeter housing is a moveable light-tight enclosure that provides sufficient cooling power to temperature stabilize the crystals, SiPMs, and amplifiers. The platform, which rides on a set of rails, allows easy insertion into or out of the ring in the radial direction. The absolute position of the calorimeter is of lesser importance than reproducibility of the position.

Several factors that influenced the technology choice are:

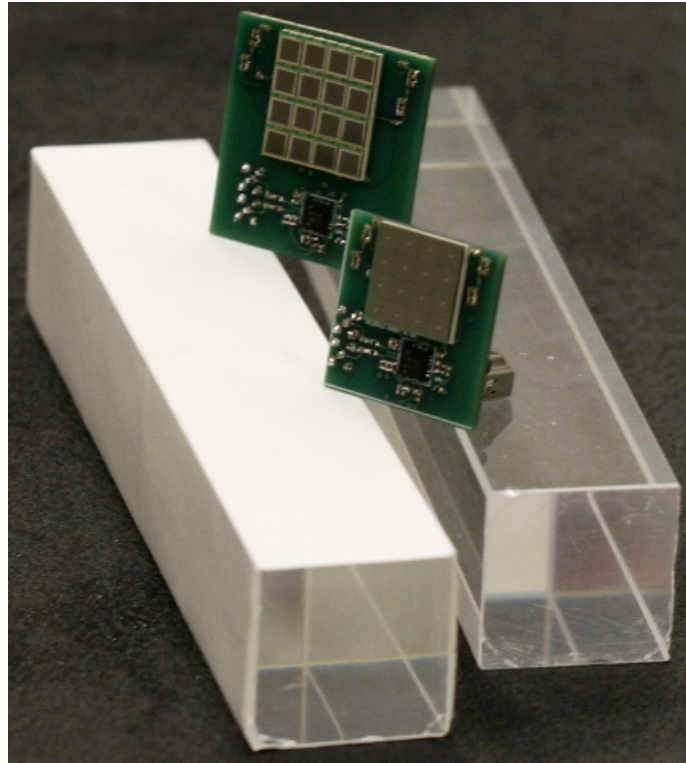


Figure 17.9: Sample $25 \times 25 \times 140 \text{ mm}^3$ PbF_2 crystals (bare and wrapped in Millipore paper) are pictured together with a 16-channel monolithic Hamamatsu SiPM mounted to our transimpedance amplifier board (front). Behind it, one of alternative SiPM designs manually assembled from 16 individual SiPMs is shown. A Millipore wrapped crystal read out by a monolithic 16-channel SiPM is the core of our recommended design.

- Each of the 24 calorimeter stations will be located in the fringe field of the central storage ring, directly adjacent to the muon storage volume in a cutout of a scalloped vacuum chamber (see Fig. 16.6). The space is highly constrained vertically (17 cm) and longitudinally (owing to vacuum interconnects and flanges). Strict limits exist on the allowed magnetic field perturbation from the absorbers, electronics and mechanical housings. All the components and materials used for calorimeter construction are carefully tested using the University of Washington test magnet.
- The absorber must be dense to minimize the Molière radius and radiation length. A short radiation length is critical to minimize the number of positrons entering the side of the calorimeter while maintaining longitudinal shower containment.
- The intrinsic signal speed must be very fast with no residuals on either leading or trailing edge since the leading edge reports on hit time, and the quality of the trailing edge is essential for reliable pileup correction.
- The energy resolution should be good—it is used to select events—but it need not be “excellent.” A resolution of $\sim 5\%$ at 2 GeV is considered sufficient and improves upon the E821 calorimeter system by a factor of 2.

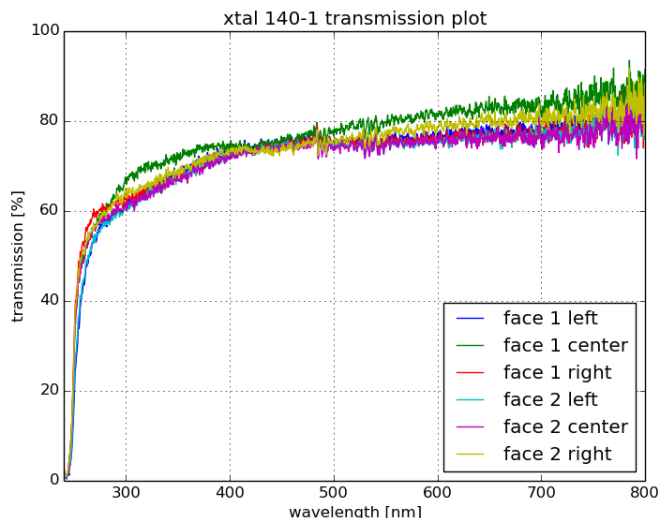


Figure 17.10: Transverse transmission efficiency vs. wavelength through a PbF_2 crystal is measured in the transverse direction. The curves correspond to transmission measurements taken with an Ocean Optics spectrometer at different locations on the crystal's faces.

17.4.1 Absorber Subsystem

The default material choice following an extensive comparative evaluation program (see Sec. 17.5) is lead-fluoride crystal (PbF_2). This crystal's combination of good energy resolution and a very fast Cherenkov signal response outperformed the other absorber options that we considered (see Sec. 18.4). It has very low magnetic susceptibility, a radiation length of $X_0 = 0.93$ cm, and a Molière radius of 1.8 cm. Our extensive test-beam program, as described earlier, verified the resolution and light yield. Table 17.2 presents a summary of the properties of the crystals.

The Shanghai Institute of Ceramics (SICCAS) provided the prototype crystals and a competitive quote for the 1325 elements required for the full system (plus spares). We own and have used instrumentation to measure the spectral response of the crystals over the range 230 nm to 800 nm, see Fig. 17.10. We have also made atomic force microscopy

Table 17.2: Properties of lead-fluoride crystals

Crystal cross section	$2.5 \times 2.5 \text{ cm}^2$
Crystal length	14 cm ($> 15X_0$)
Array configuration	6 rows, 9 columns
Density of material	7.77 g/cm^3
Magnetic susceptibility	$-58.1 \times 10^{-6} \text{ cm}^3/\text{mol}$
Radiation length	0.93 cm
Molière radius R_M	2.2 cm
Molière R_M (Cherenkov only)	1.8 cm
$KE_{threshold}$ for Cherenkov light	102 keV

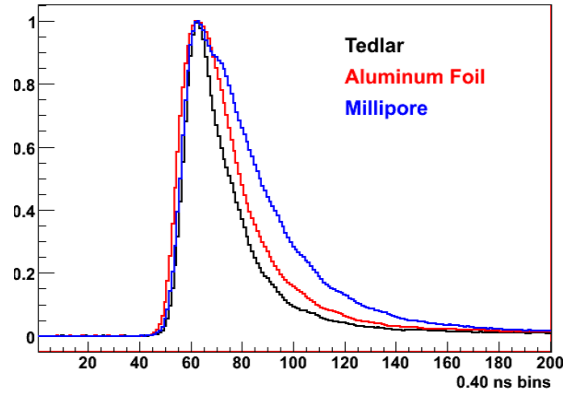


Figure 17.11: Left: Normalized response of PbF_2 crystal wrapped in absorptive black tedlar, reflective aluminum foil, and white Millipore paper. A 29-mm Photonis PMT was used to make these comparisons.

(AFM) measurements on a crystal to determine the surface quality so that we might properly represent it in our light-propagation simulations. The crystal procurement plan involves local oversight by the Shanghai University members of the collaboration, who are local to the vendor. They worked closely with SICCAS to prepare the requisition, which has now been enacted. The crystals will be sent to the University of Washington team for wrapping and assembly. PbF_2 crystals are relatively easy to handle; they are only slightly hygroscopic.

Detailed Geant4 ray-trace simulations and direct laboratory measurements have been used to study the light collection efficiency of the crystals subject to various wrapping schemes and couplings to the photo-sensitive readout. We have focussed on two extremes, namely an all-black Tedlar absorptive wrapping, and a diffuse reflective white Millipore paper wrapping. The black wrapping largely transmits only the direct Cherenkov light cone, while the white wrapping allows light to bounce multiple times within the crystals, eventually leading to a higher overall photon yield. Both wrappings have advantages, and we've

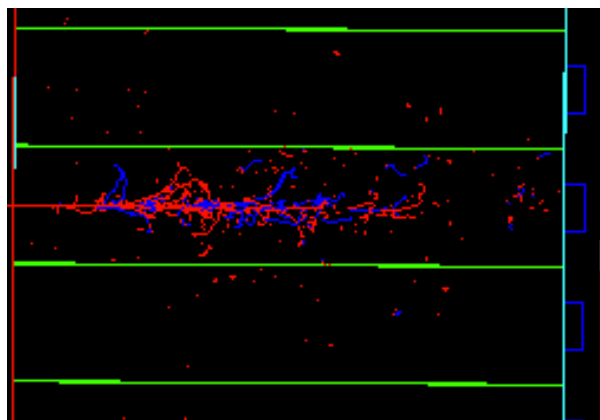


Figure 17.12: A single shower showing secondary positrons (blue) and electrons (red) in a $2.5\text{ cm} \times 2.5\text{ cm} \times 15X_0$ deep PbF_2 crystal, subject to a 2 GeV positron incident from the left. Photons have been removed for clarity.

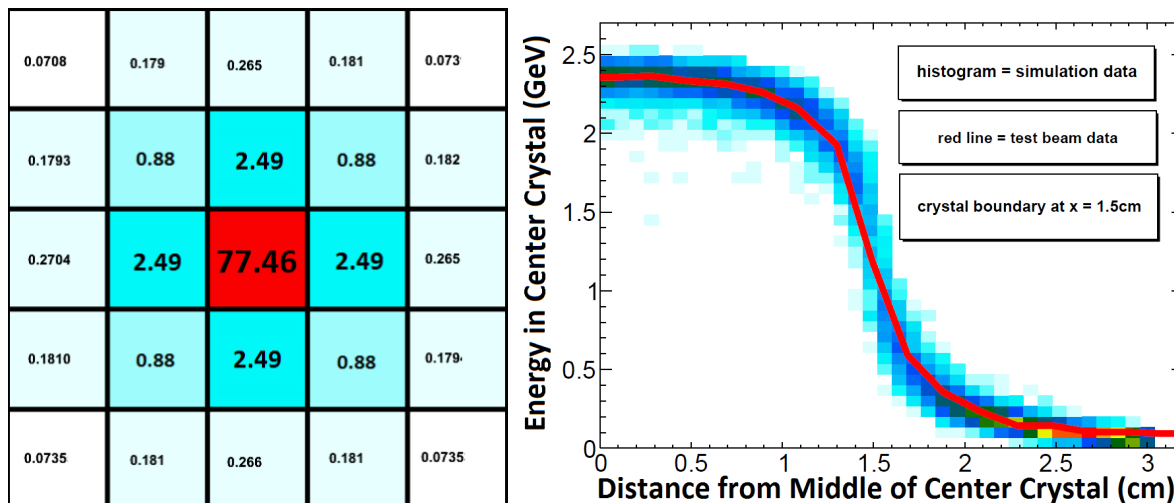


Figure 17.13: Left: Schematic representation of energy deposition in a section of the segmented electromagnetic calorimeter. Each cell is one crystal with dimensions ($2.5 \times 2.5 \times 14 \text{ cm}^3$). The numbers represent the percentage of the kinetic energy deposited in each crystal. This data was produced from a GEANT-4 simulation with a positron incident on the center of the central crystal. The results do not change for positrons in the range of 0.5 GeV to 3 GeV. Right: A comparison of test beam data and simulation data. This plot shows the shower leakage into neighboring crystals as a function of beam incidence position.

selected the white Millipore paper as our baseline choice. For the shortest pulse occupancy time, the black wrapping excels. For the greatest light yield, the white wrapping is better. Shorter-duration pulses improve pileup rejection; higher light yield improves energy resolution. We have evaluated both wrappings and an aluminum foil wrapping in a test-beam using a standard 29-mm Photonis PMT for readout. Figure 17.11 shows the results with the amplitudes normalized. The black wrapping (labeled Tedlar in the figure) response shape reached the limit of the PMT response time.

GEANT-4 simulations were used to optimize the individual crystal size and the array matrix configuration. A visualization of a typical 2 GeV positron shower is shown in Fig. 17.12. A driving specification for an array of crystals is the reduction in pileup to be realized by spatial separation. Candidate arrays of 5×7 and 6×9 (height by width) segmentation using $3 \times 3 \text{ cm}^2$ or $2.5 \times 2.5 \text{ cm}^2$, $15X_0$ -deep crystals, respectively, will fit the space constraints. A simulation with full showering and cluster reconstruction using a simple and robust two-shower separation algorithm was used to choose the best arrangement. Not surprisingly, the higher-granularity array is best. We find that it will provide at least a 3-fold reduction in pileup compared to a monolithic design. These conclusions were arrived at from a combination of simulation and direct measurement at the FTBF.

Energy sharing among neighbor crystals is shown in Fig. 17.13 for a shower that strikes the center of the middle crystal. The simulation is calibrated against the test-beam measurements in which an electron beam was directed into a crystal at various known positions and the ratio of neighboring crystal responses was recorded. Fig. 17.13 also shows a histogram of data vs. the simulation prediction. The agreement is excellent and verifies the model used

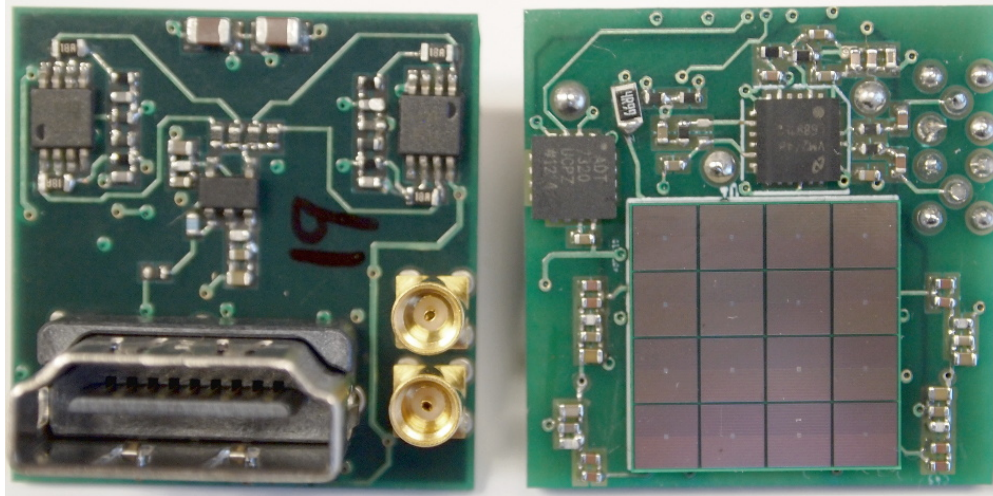


Figure 17.14: A baseline prototype of surface-mount 16-channel SiPM soldered on the amplifier board. The two MMCX connectors represent the AC coupled differential voltage signal out. The common bias voltage in, the board low voltage, and SPI lines to regulate gain are supplied through the HDMI connector.

to optimize array size and to evaluate pileup by shower separation.

17.4.2 Photodetection Subsystem – SiPM

In the baseline design, silicon photomultipliers (SiPMs) read out the crystals. While challenging and relatively new devices, they are increasingly preferred over traditional PMTs in many nuclear and particle physics applications. As such, the body of experience in their use is growing rapidly and the variety of SiPM devices from many manufacturers is increasing. They work as pixelated Geiger-mode counters. The default SiPM we are considering has 57,600 50- μm -pitch pixels on a $1.2 \times 1.2 \text{ cm}^2$ device. When a photon strikes a pixel, it can cause an avalanche that is summed together with the other struck pixels in a linear fashion to produce the overall response. Quenching resistors are intrinsic to the device to arrest the avalanche and allow the device to recover. The recovery time constant of a fired pixel is typically 10's of ns. Those pixels that are not struck, meanwhile, remain ready for a next pulse. In general, the concept is to have a pixel count that greatly exceeds the highest photon count that would strike the device. For example, for our crystals, a working number is 1.5 PE/MeV (for SiPM devices PE represents a converted photon). With a range of up to 3.1 GeV for single events, the occupancy fraction remains no more than about 5%, which is in a near-linear regime and allows for a good measurement of any closely trailing second pulse.

The selection of SiPMs over PMTs is pragmatic. SiPMs can be placed inside the storage ring fringe field, thus avoiding the awkward, long lightguides that would be needed for remote PMTs. They have high photo-detection efficiency, they will not perturb the storage ring field, and they can be mounted directly on the rear face of the PbF_2 crystals. Large-area SiPM arrays are cheaper than same-size PMTs, their cost is falling, and their performance

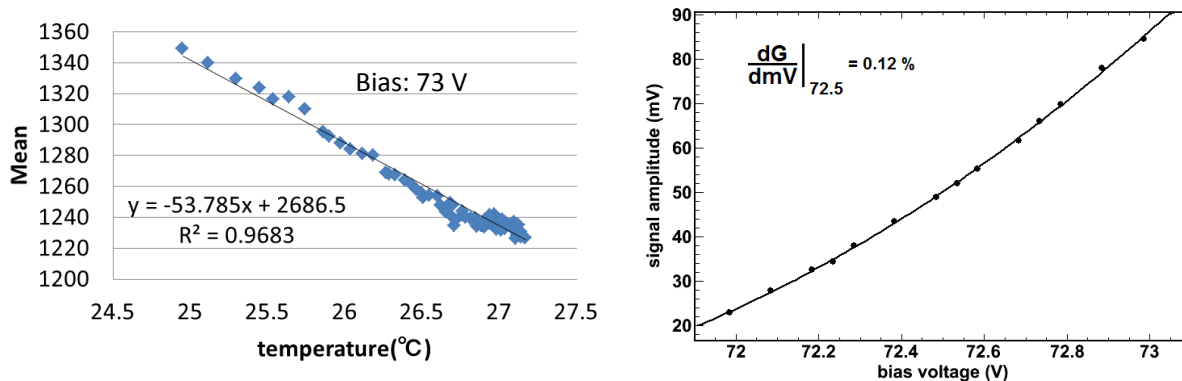


Figure 17.15: Left: Gain vs. temperature dependence of the previous generation 16-channel SiPM by Hamamatsu. Right: Gain vs. bias voltage. The measured change in gain is 0.12 % per mV.

characteristics continue to improve. We have spent the last 2 years developing lab tests to evaluate these devices. The collaboration has designed and built a series of custom pre-amplifier and summing amplifier boards. The most recent version features a multi-staged transimpedance amplifier with a remotely controllable, variable gain output state amplifier (LMH6881).

Large-area SiPM devices are packaged as arrays of smaller individual channels. While the market is constantly evolving, we are presently using a Hamamatsu surface-mount 16-channel SiPM having 57,600 $50\text{-}\mu\text{m}$ pixels in a $1.2 \times 1.2\text{ cm}^2$ active area. It is reasonably well-matched to the surface $2.5 \times 2.5\text{ cm}^2$ crystal face. Model number S12642-0404PA-50 forms our baseline design. It features Ni-based quenching resistor, through-silicon vias to avoid parasitic inductances in series with output current pulse, optical trenches to minimize cross-talk, and it is made of high-purity Si wafers to minimize dark current, after-pulsing, and to increase charge delivered by a fired pixel. Figure 17.14 shows this SiPM mounted on a prototype amplifier board.

One of the challenges of using SiPMs is their particular sensitivity to temperatures. Figure 17.15 (left panel) shows the gain change of our SiPM device vs. temperature. The gain change is 4 % per $^{\circ}\text{C}$. This measurement was performed with an older product built with a poly-crystalline Si quenching resistor. Our recommended SiPM uses a Ni-based resistor and its temperature dependence is reduced¹. The exact temperature dependence of the baseline SiPM will be evaluated during the next test run at SLAC. The calorimeter design is prepared to handle the temperature dependence currently observed. While short-term shifts are unexpected, the overall SiPM environment must be maintained at a fairly constant temperature in order to simplify the global calibration of gain during the running period.

The response of a SiPM is also quite sensitive to the bias voltage stability above Geiger-mode breakdown threshold. The right panel of Fig. 17.15 shows a lab measurement of a SiPM voltage amplifier board output vs. bias voltage. The slope is gain is 0.12 % per mV

¹The Ni fraction is tiny; we evaluated the magnetic perturbation of this SiPM in our test magnet and the effect of Ni is negligible.

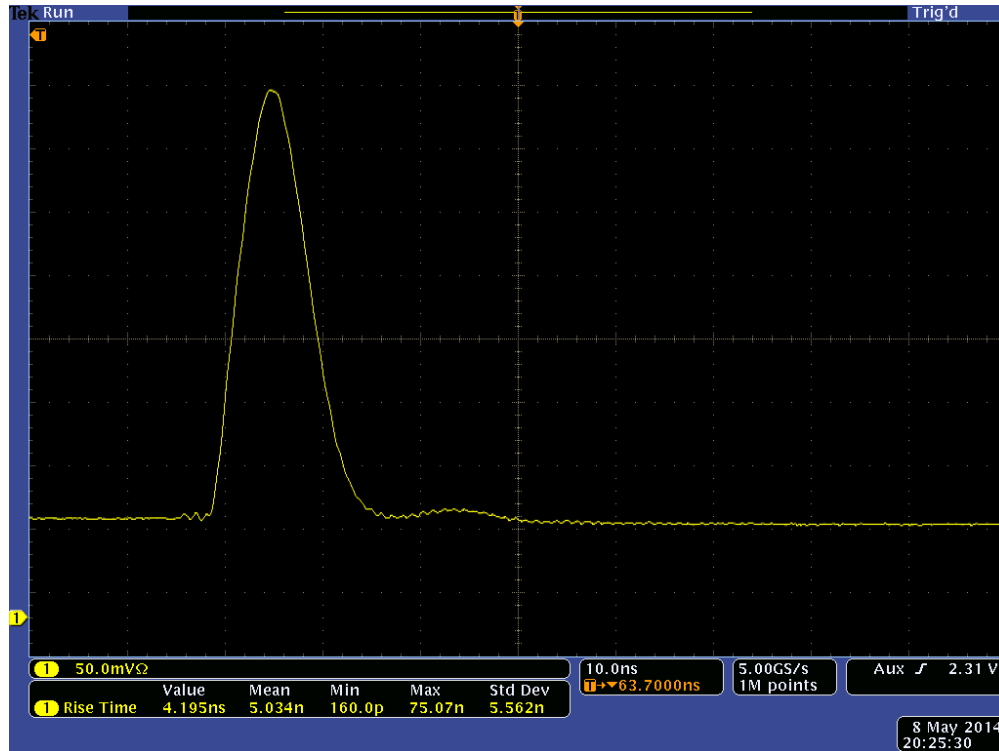


Figure 17.16: A scope trace of the SiPM response to a 2.5 ns wide LED pulse. For the purpose of the measurement, a balun transformer was used to convert the differential output into a single ended one.

near the working bias of 72.5 V, leading to the need to have a separate bias control subsystem, which we describe in Subsection 17.4.2.

The most recent amplifier board (Fig. 17.14) is based on a concept of a multi-staged, transimpedance op-amp. In the first step, current pulses from 4 SiPM channels are added together and converted into voltage pulses in a fixed-gain transimpedance amplifier which is operated at a constant gain of $600\ \Omega$. This first stage is designed around a THS32302 op-amp, which is operated in current mode. Avoiding any shunt resistors, extremely low input impedance of the op-amp, and 2 GHz bandwidth are keys to short pulse widths. In the next step, the four partial sums are added together using a THS3201 op-amp operated at unity gain in voltage mode. The final stage drives an AC coupled differential pair of coax cables, and is designed around a LMH6881 digitally controlled variable gain amplifier. A 2 V_{pp} amplitude at the output of the amplifier board corresponds to energy deposited in the crystal by a 4 GeV positron. A representative pulse shape response to a 2.5 ns-wide LED pulse is shown in Fig. 17.16. The pulse FWHM here is ~ 8 ns.

Given this working electronics board, measurements were carried using our fast laser system (pulse width < 1 ns) to determine the two-pulse separation and the sensitivity to high rate. A scope shot of two such pulses, separated by 8 nsec is given in the right panel of Fig. 17.17. These pulses can be easily resolved in a fit. The left panel demonstrates that the SiPM board is capable of operating well at a rate of 10 MHz. These and other test to date show that the current design meets the demands of the experiment.

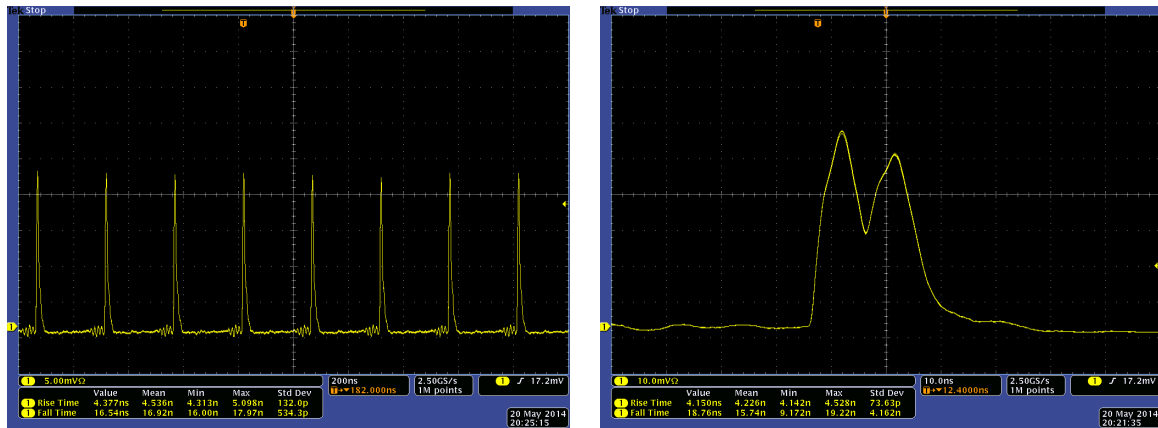


Figure 17.17: Left: A baseline SiPM prototype is stable running under 10 MHz laser shots. Right: An example what a SiPM response to a 8 ns pileup looks like.

Bias voltage system for the SiPMs

Several possible approaches and technical implementations have been considered for the SiPM Bias Voltage System (BVS). In the initial stages of the E989 proposal and instrumentation development, the only viable option was a dedicated design and fabrication of modules specific to this experiment. None of the commercially available units at the time was able to produce the combination of specifications thought to be required for the E989 Calorimeter SiPMs: 1 mV or better precision of setting and stability of maintaining bias voltages in the 60–80 V region, while maintaining a time-average current of $\sim 50 \mu\text{A}$ for each channel, with significantly higher instantaneous peak currents associated with storage ring filling times. Each channel was expected to require its own distinct value of bias voltage, accurately maintained over time.

Two prototype designs were developed at the University of Virginia, and four 16-channel BVS boards were built and instrumented in a dedicated chassis jointly with the group from James Madison University. The prototype systems were operational in June 2014, and were tested in-beam during a test beam time at SLAC in July 2014. Sadly, both designs turned out to suffer from instabilities and bias voltage variation with load far outside the specified limits, requiring a thorough redesign.

At the same time, evolution in the design and production of the Geiger-mode avalanche photodiodes have resulted in significant changes in requirements for E989 Calorimeter BVS. The main result of these developments is that more recently produced batches of SiPMs cluster far more narrowly in gain and bias voltage requirements than the older units did.

On the other hand, in-beam as well as laboratory laser tests and evaluations of recent generation SiPMs have yielded wider plateaus of acceptable gain vs. bias voltage, relaxing the narrow requirement for bias voltage compared to the initial specifications.

Thirdly, in 2015 manufacturers iseg/Wiener and CAEN introduced several new high precision high voltage modules with increased stability, as well as high delivered current, 10 mA or more per channel. These modules make it feasible to design a central calorimeter bias voltage system in which typically some 12 channels share the same bias voltage. This drives down channel multiplicity and cost by an order of magnitude. The location of the

system in the center of the storage ring further reduces the risk that the BVS would affect the storage ring magnetic field, thus removing the need for extreme control of magnetic properties of each component in the system.

At the time of this writing we are testing three modules: iseg EHS 8401pF, Wiener MPV8120LI, and CAEN A1539 in their respective MPOD and CAEN chassis enclosures. They were delivered to the University of Virginia in the last week of May (iseg/Wiener) and April (CAEN). All are capable of delivering 10 mA per channel, or more, and thus provide a large current reserve even if each channel is split among as many as 12 Calorimeter modules. Following basic bench-top tests, the units will be tested with an array of calorimeter crystals and SiPMs, along with the E989 laser pulsing system.

Initial tests indicate that all units maintain stability at the sub-mV level, which provides a solid foundation for a BVS system that meets all E989 requirements. The iseg/Wiener units have the advantage of having individual isolated grounds for each channel, an essential feature to prevent the occurrence of ground loop noise. The realistic tests with calorimeter module array(s) will determine what modifications, if any, are needed on the breakout boards in order to ensure that they provide the charge locally to each channel on the μs time scale, to accommodate the transient current draw associated with storage ring filling times.

17.4.3 Laser Calibration System

A high performance calibration system is required for the on-line monitoring of the output stability of each individual tower in all calorimeter stations. It is estimated that the detector response must be calibrated with relative accuracy at sub-per mil level to achieve the goal of the E989 experiment to keep systematics contributions to the accuracy on the measured observables at 0.02 ppm level. This is a challenge for the design of the calibration system because the desired accuracy is at least one order of magnitude higher than that of all other existing, or adopted in the past, calibration systems for calorimetry in particle physics.

Almost 1,300 channels must be calibrated during data taking; the proposed solution is based on the method of sending simultaneous light calibration pulses onto the readout photo-detector through the active sections (crystals) of the calorimeter. Light pulses must be stable in intensity and timing to correct for systematic effects due to drifts in the response of the crystal readout devices. A suitable photo-detector system must be included in the calibration architecture to monitor any fluctuation in time of the light source intensity and beam pointing as well as any fluctuation of the transmitted light along the optical path of the light distribution system, which could occur due to mechanical vibrations or optics aging.

Some guidelines are defined to select the light source(s) and to design the geometry of the light distribution and monitoring; the following criteria are adopted to select the light source type:

- light wavelength must be in the spectral range accepted by the detector and determined by the convolution of the spectral density of the Cherenkov signal produced by electrons in PbF_2 crystals with the spectral transmission of the crystals, and with the spectral Q.E. of the photo-detector; Q.E. is peaked around 420 nm for SiPMs.
- the luminous energy of the calibration pulses must be in the range of the electron deposit in the crystals, typically 1-2 GeV; this corresponds to a luminous energy on

each tower of a calorimeter station of about 0.01 pJ, or to about 13 pJ for simultaneous excitation of all calorimeter readout channels (1300). The numbers quoted above merely indicative of the order of magnitude and they are derived by assuming that the readout of each crystal will produce about 1.5 photo-electrons per MeV with 30% P.D.E. (Particle Detection Efficiency) for SiPMs and with 23% coverage of the crystal readout face.

- the pulse shape and time width must be suitable to infer on the readout capability in pile-up event discrimination; pulse rise/trailing time must be of the order of some hundred of picoseconds, the total pulse width should not exceed 1 ns. This implies a peak power per pulse at the source of some Watts (some nJ in a 1 ns wide pulse), assuming the conservative value $0.001 < T < 0.01$ for the total intensity transmission factor of the calibration system.
- the pulse repetition rate must be of the order of 10 KHz; this value will be tuned to obtain the best compromise between the need of having enough calibration statistics in the time interval (some tens of microseconds after the muon injection in the ring) when the maximum rate is achieved in the readout devices and the need to avoid saturation of the DAQ bandwidth.

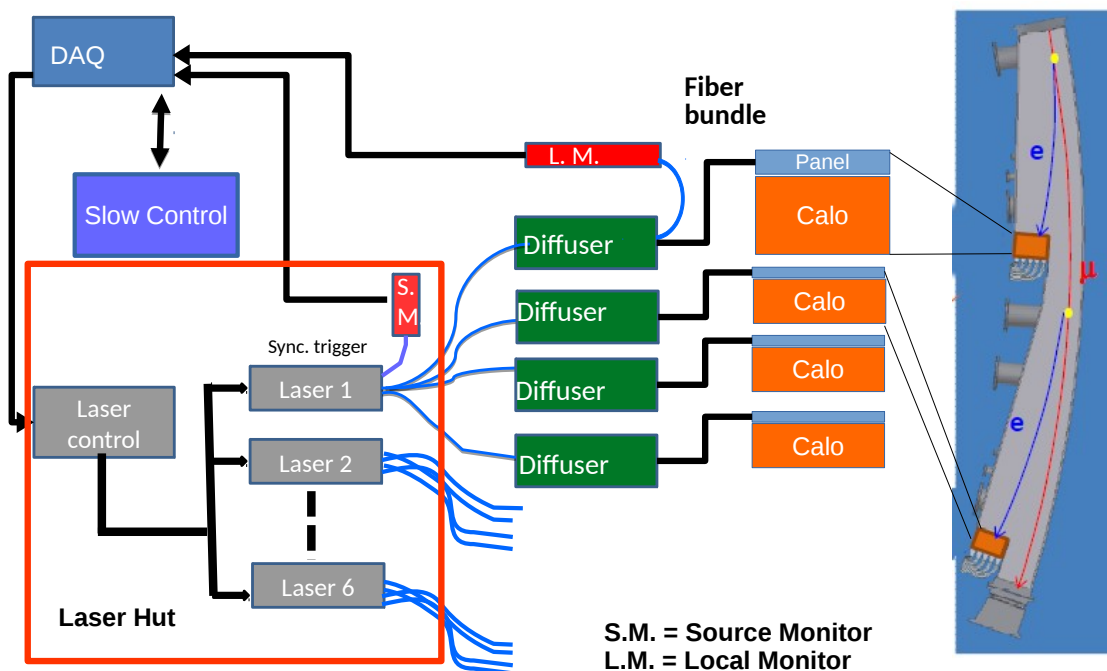


Figure 17.18: Sketch of the laser calibration system of the calorimeter.

A number of commercial diode lasers, for example LDH series from Picoquant, bare diodes from Roithner LaserTechnik, Picopower-LD series by Alphalas or others, cope with the criteria listed above and have been considered as a source for the calibration pulses. The final choice will be made after the completion of all tests required to qualify, in terms of light transmission and time stability, all other optical elements of the calibration system. Guidelines for designing the light distribution chain are listed below:

- High sensitivity monitors of the transmitted light at the end-point of each individual section of the distribution chain must be used to ensure online control of the system stability and to have information for applying feed-back correction to the source operation parameters, if needed.
- The optical path must be minimized in order to limit the light loss due to self-absorption in the optical fibers. The number of cascade distribution points must be also minimized to reduce the unavoidable light loss in the couplers between different sections.
- The laser source and its control electronics should be located outside the muon ring in order to avoid e.m. perturbations of the local field induced by the current flow used to excite the laser. Consequently, a suitable geometry should include: 1) a primary light distribution point outside the ring, 2) a number of silica launching fibers about 20 meter long, used to feed light from the primary distribution point to the secondary ones, and 3) secondary distribution points located close to each calorimeter station. From the secondary distribution points, short bundles of plastic (PMMA) fibers, about 1 meter long, feed the light through a panel to each individual tower. of the calorimeter station.
- Optical fiber selection: multimode silica fibers (20 dB/Km attenuation at 400 nm) are the best solution for long path light transmission and in terms of robustness against solarization or other aging affects due to large values of transmitted light intensity. For the shorter fiber bundles, where the transmitted intensity is at least one order of magnitude lower and the distance to be covered very short, PMMA fibers (200 dB/Km attenuation at 400 nm) are considered, also for budget reasons.

A possible geometry fulfilling all the requirements set by the guidelines listed above is shown in Figure 17.18. The light generated by the laser source (a pulsed diode laser) is divided in 4 or more parts, coupled into the launching fibers and sent to the secondary distribution points located inside the ring and near each calorimeter station. A battery of 6 synchronized lasers will be necessary to provide the required light power. They will be located, together with the optics and the fiber couplers, onto an optical table inside a laser hut with temperature and dust controls. The quartz launching fibers (about 20 meter long, one per calorimeter station) route the light to secondary distribution devices located near the calorimeter stations, each distributor serving one station. A small fraction of the light exiting each laser source and each light distributors is routed to source and local monitors respectively. Their analog signal is returned to the DAQ system for both on-line checking of the system stability and further offline monitoring of the calibration signal. Interface with DAQ is also required for slow control signal recording and communication with the timing signal controls is used to trigger the electronics of the laser driver. The monitors are designed

to factor out instabilities in the laser system: assuming the laser-induced signals from all calorimeter elements (Sci) and the monitor (SM) are subject to the same laser fluctuations, the fluctuations should be eliminated in the ratio Sci/SM . These ratios should then reveal fluctuations in the calorimeter response, provided other fluctuations in SM are stable to the degree required.

The following approach is considered to optimize the monitor stability:

- We use zero gain PIN diodes which are much more stable than SiPMs to variations in bias and temperature;
- We expose them to much higher light levels to minimize photostatistical fluctuations;
- We equip the monitor with electronics specifically designed to get high stability. This electronic board is currently under construction;
- We use a redundant system, with two photodetector for each monitor;
- We minimize pointing fluctuations by incorporating diffusion and mixing elements;
- We incorporate a radioactive source, for absolute calibration.

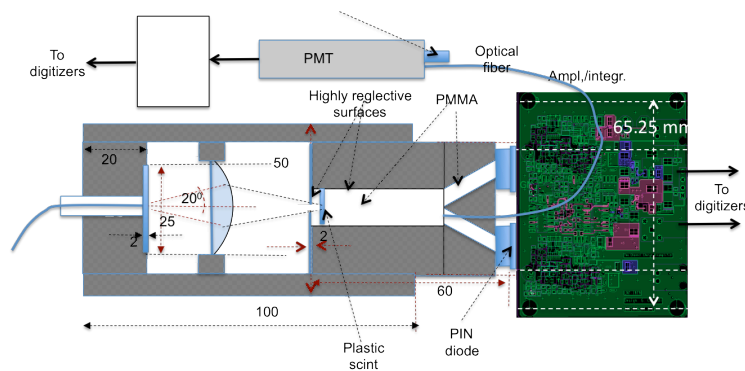


Figure 17.19: Schematic illustration of the monitor prototype.

Based on these consideration, a monitor prototype (whose geometry is sketched in Figure 17.19), has been developed.

The laser light is injected by a fiber from the left and is incident on a diffuser engineered to emit in a 20° angle. The diffused beam is focused onto fast plastic scintillator disk located near the entrance to a diffusing chamber and faced up against a PMMA mixer. The fast scintillator acts as an ideal diffuser because it emits isotropically. The cavity filled with PMMA acts as a mixing chamber. This combination should be effective in minimizing beam-pointing fluctuations which could be produced by fluctuations in the emittance of the laser. The photodetectors include two large-area PIN diodes for redundancy. The PIN diodes are relatively slow (~ 10 ns pulse width) compared to the laser pulses but fast enough given that they will be integrated by their electronics for stability. The third photodetector is a PM with a 8 mm diameter cathode and a Cockroft-Walton base which generates its own HV and operates at low voltage. Laser fluctuations are eliminated in the ratios of these

three signals which are used monitor other eventual instabilities in the individual signals. PM stability is monitored independently by exposure to the signal from a NaI crystal on which a very small quantity (~ 10 counts/sec) of ^{241}Am has been deposited. Since the PM is also sensitive to the laser signals it serves as an absolute reference. The prototype of the preamplifier/integrator card for the PIN diode signals, currently under development, is also shown in Figure 17.19.

Qualification tests of the individual components, including comparison measurements of different options, have been extensively performed:

- laser source: as an alternative to a single, powerful laser light source, the possibility to use four or six synchronized laser heads with lower power (diode lasers), controlled by the same driver has been chosen. This solution has the advantage that, in case of one laser failure, no calibration stop will occur during data acquisition. Moreover, pulsed diode lasers have excellent stability characteristics and versatility in driving rates.
- light distributors: baseline solution uses simple beam splitters and coupling into multimode launching fibers. This solution should guarantee intensity stability of the distributed light against geometrical effects due to beam-pointing instabilities. Beam splitters made with the linear circuit technology could also be considered as primary distributors if commercial devices, nowadays widely used only in the IR range for telecommunication, will be produced for the near-UV/visible range. A prototype will be tested soon. Concerning secondary distributors, extensive tests have been performed to compare an integration sphere versus an engineered diffuser. The former shows a higher degree of output uniformity (up to 99.3 percent for a 1 mm diameter fiber connected to one sphere port) at the price of a higher factor in intensity loss. The latter shows a satisfactory degree of uniformity (see Figure 17.20) with a much higher transmission factor and has been retained for the baseline solution of the light distribution system. The comparison between the integrating sphere and the engineered diffuser has been published in Ref. [7].

The complete chain of the baseline solution of the distribution system, from the laser head to the single calorimeter tower, has been tested experimentally by sending laser signals to the rear faces of the PbF_2 crystals, where the SiPM photodetectors are placed. Here, one important requirement for the laser calibration pulses, beyond stability, is uniformity. In our baseline system, the light from the 54 plastic fibers of the bundle is reflected inside a panel placed in front of the calorimeter (see Fig. 17.18) and sent into each tower. The uniformity of the illumination of the rear facet of the PbF_2 crystal is shown in Fig. 17.21, where a continuous wave laser at 532 nm has been used. The obtained uniformity is enough to ensure a comparable illumination of all SiPMs in the calorimeter station, which have a surface covering only 23% of the crystal faces and, due to mounting constraints, are not placed in the same position with respect to the crystal axis.

17.4.4 Mechanical Subsystem

Each calorimeter station will comprise a number of individual crystals that are made out of dense, usually brittle, material. In addition, the detector including the photo-sensitive SiPM

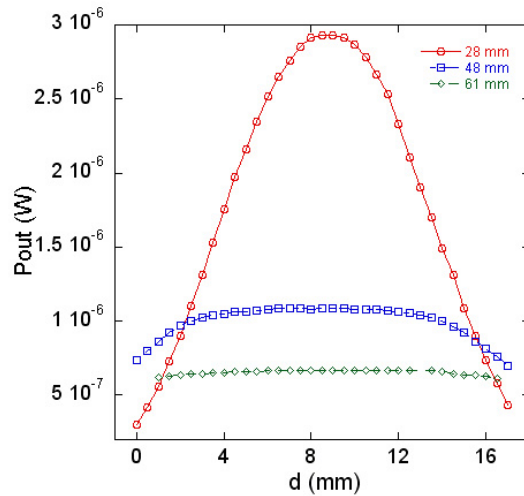


Figure 17.20: Mapping of the illumination uniformity after the 20 degrees diffuser. The light is collected with a 1 mm diameter, 0.49 N.A. optical fiber, at different distances from the diffuser. The input power on the diffuser is 1.3 mW.

must be in a light tight encapsulation. A set of crystals and photo-detectors forming one calorimeter station weighs ~ 40 kg. The housing must provide the light tightness, proper stability to carry the weight, feedthrough for bias and low voltage, and a mechanism for easy lifting of the entire box and insertion into or out of the ring in the radial direction.

The locations of the 24 calorimeters in the experiment are fixed by the design of the scallop-shaped vacuum chambers. Several vacuum ports, bellows and the magnet's pole gap impose spatial limitations on the design. Specifically, the length of the calorimeter station along the positron's trajectory cannot exceed 38 cm. The pole gap limits each station to less than 17 cm. There are no tight limiting factors in the radial dimension that we can see would constrain the calorimeter station.

For installation, maintenance and access to the vacuum chamber or the magnet, each calorimeter station must be easily removable. We will determine later the degree of alignment necessary, but a system of pins should allow for a reproducible position. The absolute position is less critical. The calorimeter housing and retractable platform must allow for routing of a variety of cables (detector signals, bias voltage, control signals, monitoring signals) and service lines (e.g. cooled air pipes). The mechanical design must incorporate space for the readout electronics crates to be placed on-board to be compatible with the moving mechanism.

Heat dissipated by a SiPM and its amplifier board is removed by dried cool air. The maximum heat power under a steady very high rate hypothesis (very long high rate laser run) could reach up to 1.2 W per SiPM board. The cooling system is design with a power

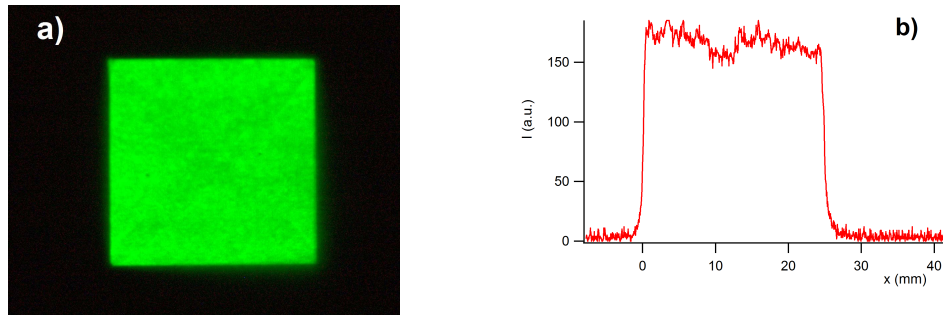


Figure 17.21: In a) image of the laser light exiting the rear facet of the crystal, diffused by a paper sheet. In b) Horizontal cut of the image in a).

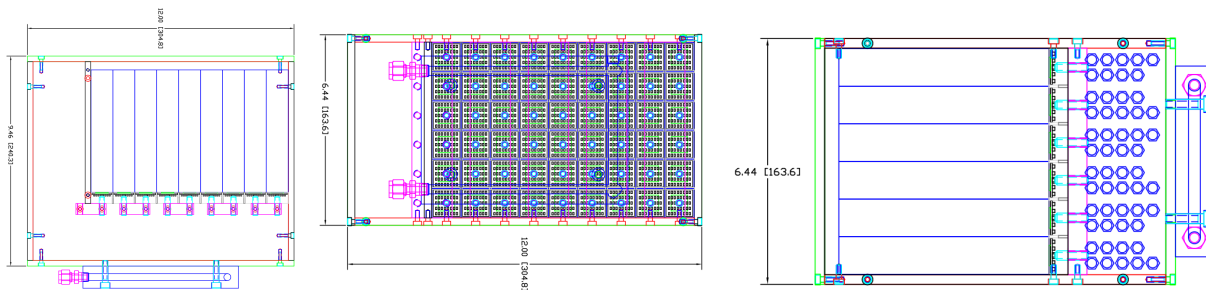


Figure 17.22: Proposed calorimeter light-tight housing. Left: Top view of 9 crystal columns. The storage ring is on the right. The extra space on the left side is used for panels, cooling, servicing. The rear part of the box includes a cooling channel. The front accommodates the calibration plate (not shown here). Middle: Side view of 6 rows of crystals. The conceptual plan for the chicanes where signal cables pass through is indicated. Right: Rear view showing the 54 SiPM amplifier summing boards.

limit of 2W in mind, and was successfully commissioned during a SLAC run. The system consists of a small cooler serving as a source of cooling power for pressurized air dried in a large desiccant container. A distribution system delivering a steady flow of cool air directly to the center of a SiPM board forms the back wall of the calorimeter box.

A mechanical housing system was built for the test beam and a full-scale version has been designed by CENPA engineers and costed for the experiment. It ensures a light-tight environment, provides cooling as necessary for stable SiPM board operation, includes patch panels and chicanes for cable runs and has a front-end that will mate to the calibration interface plate described in fig. 17.23. The housing has serviceable doors that will allow easy access to the crystals and readout devices. Figure 17.22 shows three engineering drawings of the proposed system. The front panel of the light-tight housing holds the calibration plate. Figure 17.23 shows our current design in perspective.

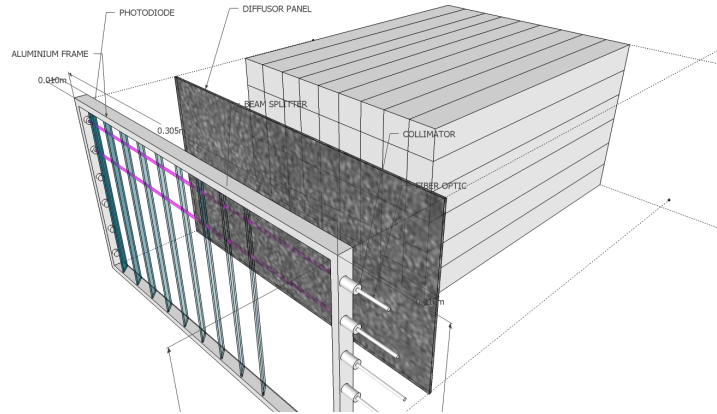


Figure 17.23: Proposed front calibration plate. Six optical fibers penetrate from the inner radial direction. The light is split using a series of beam splitter plates. An alternative design based on a diffuser panel that spreads the light across the crystal front faces is obsolete now.

17.5 Alternative Design Considerations

Two alternative calorimeter material options and one alternative readout option were tested. These included a home-built tungsten-scintillating fiber sampling calorimeter, which is dense ($X_0 = 0.7$ cm), and has a fast-scintillator signal response [2]. Unfortunately, it did not exhibit acceptable resolution in the as-built W:SciFi 50:50 ratio and necessary modifications would reduce the density. Next we tested a custom undoped lead tungstate (PbWO_4) crystal. The idea was to reap the benefits of the higher light yield of PbWO_4 , but to avoid the slow scintillator light component that is prohibitively long for our application. Although its resolution was excellent, the intrinsic pulse FWHM of 15 ns greatly exceeds the 4 ns width measured for PbF_2 . There were no benefits of this crystal from cost or other perspectives. The choice of absorber is fixed. Owing to the long lead time and proven design, we have ordered the crystals for $g - 2$. The decision has been taken.

We also evaluated fast photo-multiplier tubes as alternatives to SiPMs. The Hamamatsu 9800 is an excellent PMT, having a fairly compact footprint and intrinsic fast response. We are using it regularly to benchmark the intrinsic light output time distribution from our crystals. Unfortunately, it is not a good choice for full implementation in the experiment owing to the need to place these PMTs at least 1.5 m from the calorimeter arrays. Because of the rear-face readout from the geometry, the guides would require a rapid 90-degree bend toward the radial direction and then a second bend to put the PMTs out of plane. The high cost of the PMTs (about 5 times higher than the SiPMs) and the awkward light-guide constraint were deemed to be major issues compared to the development of SiPMs that can be located onboard the crystals. Turning now to a PMT-based solution would increase costs significantly and introduce delays, as the design and testing program would have to start anew for this option. We have committed to using on-board, non-magnetic, fast SiPM readout.

One option to increase the fractional readout area on the rear face of the crystals (presently $144 \text{ mm}^2 / 625 \text{ mm}^2$ for the 16-ch MPPC) is to use larger area arrays of tile-able SMT packaged SiPMs on custom-designed PCBs. For example, an ideal 5×5 array of

9 mm² can be made using single channel Hamamatsu devices. Larger area coverage would allow the use of smaller, thus in principle faster pixels, while maintaining sufficient overall photon detection efficiency. We built such a 16-channel segmented SiPM board from 25 μm products and evaluated against a monolithic 50 μm pixel board. They turned up having exactly the same pulse shape width. The sub-optimal leads that the small product comes with suffer with high parasitic capacitances that deteriorates pulse shape. Also manually assembled SiPM board is significantly more expensive and the cost per unit area of the SiPMs packaged in these smaller units is nearly a factor of two higher.

17.6 ES&H

The 1300 SiPMs all receive a low-current (limited to 150 μA) \sim 70 V bias voltage, which is delivered to the enclosed housing through ribbon cables from a custom-built bias control system.

A laser system will be used to distribute calibration pulses. Apart from the laser hut, the light will be entirely contained in optical fibers, with no possibility of escaping under normal use. The laser hut will be located in the electronics control room and will have appropriate FNAL-supported safety and security requirements included and proper training for any operators.

The mechanical weight of the calorimeters is only 40 kg each and they will be supported on railed housings. There is no vacuum insertion, but these detectors will be placed near the storage ring magnetic field and, as such, care must be taken when servicing them to ensure that no magnetic tools are used (a general requirement for any access to the storage ring area).

17.7 Risks

17.7.1 Performance Risks

In the very unlikely case that the gain stability of the system in actual use fails to meet the specifications, other analysis techniques will have to compensate for the energy scale information loss. This situation happened in E821, where the laser system did not meet the performance goals. Instead, E821 was able to determine the stability of the gain from the data itself. It is not ideal, but did mitigate the risk.

17.7.2 Schedule Risks

An NSF Major Research Instrumentation proposal was granted in 2013 to a consortium of six domestic and one international partners within the full collaboration. A substantial matching component was arranged from the domestic and international universities involved. The MRI funds provide already the full necessary capital to fund the detectors, electronics and DAQ systems related to the measurement of the muon precession frequency, ω_a . This funding supports the purchase of all PbF₂ crystals, the SiPM readouts, the board fabrication and design, and the mechanical housing, as described in this Chapter.

In early 2014, the contract for the purchase of 1325 PbF₂ crystals from the Shanghai SICCAS High Technology Corp was completed. The first batch of 25 crystals was received in May, 2014.

Separately, the Italian groups were granted partial funds, and are awaiting approval for the rest of resources from INFN for their production of the calibration subsystem.

Since the MRI funds were secured, all associated funding-based schedule risks are extinct. The demanding performance parameters applied to the bias control and laser gain monitoring system could require revision cycles that impact the schedule. We are mitigating the risk with an aggressive R&D program schedule that will accommodate several design iterations.

17.8 Quality Assurance

Our local Shanghai University collaborators are able to monitor the production of the crystals at SICCAS and intervene if any problems arise. The crystals will be shipped to the University of Washington where they will be measured, and tested for transmission efficiency, then wrapped. A traveler document system has been written to keep track of crystals and measurements. The SiPM boards will be built and then tested using a custom light scanner that can calibrate each device. Finally, the individual crystal-SiPM packages will be assembled into an array and tested with a calibrated laser front panel plate. We have a SiPM test laboratory at UW to evaluate the production SiPM boards and will prepare a program using undergraduate students to evaluate each piece in the assembly line.

17.9 Value Management

Competitive quotes had been obtained in order to prepare the MRI Proposal. Local fabrication at universities with largely overhead-free labor will keep costs in check. We have finished an aggressive program of SiPM vendor evaluations and board designs to maximize readout coverage at competitive cost.

17.10 R&D

We have used test beam opportunities at Fermilab and SLAC repeatedly as necessary. We intend to return to SLAC for another electron test beam to demonstrate calorimeter performance and long gain stability with prototypes of the final HV power supplies and digitizers.

We continue to use our local laboratory tools to evaluate SiPM performance and have several student projects ongoing to map out gain functions and other performance characteristics.

References

- [1] S. A. Sedykh *et al.* Nucl. Instrum. Meth. A **455**, 346 (2000).
- [2] R. McNabb *et al.* Nucl. Instrum. Meth. A **602**, 396 (2009). arXiv:0910.0818 [physics.ins-det].
- [3] A. T. Fienberg *et al.* Nucl. Instrum. Meth. A **783**, 12 (2015). arXiv:1412.5525 [physics.ins-det].
- [4] P. Achenbach *et al.* Nucl. Instrum. Meth. A **465**, 318 (2001).
- [5] V. Tishchenko *et al.* [MuLan Collaboration], Phys. Rev. D **87**, 052003 (2013). arXiv:1211.0960 [hep-ex].
- [6] L. P. Alonzi [Muon g-2 Collaboration], Calorimeter Acceptance, (2014). $g - 2$ internal document: <http://gm2-docdb.fnal.gov:8080/cgi-bin/ShowDocument?docid=1838>
- [7] A. Anastasi *et al.* Nucl. Instrum. Meth. A **788**, 43 (2015). arXiv:1504.00132 [physics.ins-det].

